Title

The use of a digital micromirror array as a temporal gate and spatial-filtering device for laser-induced breakdown spectroscopy and laser ablation molecular isotopic spectrometry

Authors

Williams, Kelsey L
Chan, George C-Y
Ray, Steven J

Publication Date

2021-05-01

DOI

10.1016/j.sab.2021.106116

Peer reviewed

The Use of a Digital Micromirror Array as a Temporal Gate and Spatial-Filtering Device for Laser-Induced Breakdown Spectroscopy and Laser Ablation Molecular Isotopic Spectrometry

Kelsey L. Williams[1], George C.-Y. Chan[2], and Steven J. Ray[1*]

[1]The State University of New York at Buffalo, Buffalo, New York 14260, United States

[2]Lawrence Berkeley National Laboratory, Berkeley, California 94720, United States

* Author to whom correspondence should be addressed: sjray2@buffalo.edu

ABSTRACT

A digital micromirror array (DMMA) is used in a simple and inexpensive approach for spatially resolved temporal gating of atomic emission detection in laser-induced breakdown spectroscopy (LIBS). Selected mirrors in the array are actuated at a time delayed from the primary laser pulse, permitting optical gating with a response time of 160 ns while using a conventional CCD detector. Detector gating is shown to decrease noise from short-lived spectroscopic background (both continuum and N II from air), improving signal-to-background ratios by 22-times for selected samples and emission lines. The utility of rapid temporal gating is also demonstrated for the optical detection of isotopes using the laser-ablation molecular isotope spectrometry (LAMIS) experiment. Optical temporal gating and spatial filtering are used to isolate regions of the laser-induced plasma, enhancing signal from molecular emission. The potential of the simple technique for use in field-portable LIBS and LAMIS experiments is explored.

1. INTRODUCTION

The spectroscopic signal in laser-induced breakdown spectroscopy (LIBS) has a well-known temporal dependence. Broadband spectral background resulting from bremsstrahlung radiation and electron-ion recombination is intense for a time immediately following the incoming primary laser pulse, but then dissipates over a timeframe of microseconds [1]. Since atomic emission is longer-lived, the optimum signal-to-background ratio (S/B) and signal-to-noise ratio (S/N) are achieved by delaying detection from the initiation of the laser plasma. Similarly, a relatively new method of performing isotopic analysis via optical spectroscopy known as laser ablation molecular isotopic spectrometry (LAMIS) also relies upon gated detection of emission [2]. LAMIS exploits the isotopic wavelength shift of molecular emission from diatomic molecules that are formed in the aftermath of a LIBS plasma in order to measure isotopic ratios of elements within a sample. Interaction of analyte atoms or ions with ambient gases (mainly oxygen and nitrogen) results in formation of these excited diatomic molecules, and thus emission from these condensed species are detected with optimum S/B at time delays greater than those used in LIBS [3]. Atomic and molecular emission from LIBS and LAMIS plasmas also have distinct spatial patterns, for example, short-lived ionic emission and longer-lived atomic emission are most intense in the central portion of the LIBS plasma [4]. Molecular emission is most intense at the interface between the plasma and ambient atmosphere, at the edges of the plasma boundary [5, 6]. These observations suggest the need for spatial filtering and temporal gating for LIBS and LAMIS experiments to obtain optimal S/B.

A variety of strategies have been used to gate optical detection in LIBS [7-10]. Intensified charge coupled devices (ICCDs) offer wide wavelength response with temporal gating on the order of nanoseconds. However, ICCDs are also expensive and fragile, and despite

the high gain of ICCDs, a number of studies have shown that the S/N achieved using ICCDs can be comparable to those achieved using conventional CCDs when used for LIBS detection [10-12]. Because the main drawback of using a conventional CCD for LIBS is the lack of rapid temporal gating, several temporal gating approaches have been examined. Acousto-optic modulators have been used to gate CCD integration with gate delays on the order of 200 ns, however, nearly 80% of the light emitted by the LIBS plasma was lost when using this approach [13]. Mechanical choppers have also been used with CCDs to achieve gate delays and widths from 1 ms – 200 ns however, mechanical chopper disks have a set form that is not easily changed and can deform, making on-the-fly gating changes and calibration especially difficult [10, 11].

In addition to time-resolved optical detection, spatially resolved imaging of the laser-induced plasma is often used to study plasma conditions and chemistry that takes place within the LIBS plume. The techniques used vary depending on the information being acquired. Spatial dependence of emission lines can be used to determine local plasma temperatures and number densities by simply using micrometer stages that allow for precise spatial positioning with respect to the optical sampling volume [4, 6]. Spatial discrimination of plasma emission can be achieved by using a fiber bundle to guide light from specific locations to the slit of the spectrometer [5]. Often, imaging of the entire plume is important, such as in visualization of the shockwave from the LIBS/LAMIS event by shadowgraphy [6].

Here we explore the use of the digital micromirror array (DMMA) as a device for temporal gating and spatial filtering for LIBS and LAMIS detection using a conventional CCD detector. The DMMA is a micro-electro-mechanical system (MEMS) that is comprised of an array of individually controllable mirrors. Each mirror can be tilted ±12° with respect to the

mirror perpendicular in 5 μs, allowing for redirection of light and formation of an image using a user-defined mask (*cf.* Figure 1A). These devices are commonly found in commercial electronics (e.g. projectors), but have found their way into spectroscopic applications such as hyperspectral imaging [14], maskless photolithography [15], and atomic spectroscopy. Spudich and co-workers used a DMMA as a multiplexer for spectroscopy, such as in multi-element detection in atomic absorption spectrometry [16]. Batchelor and Jones used a DMMA to scan between wavelengths for detection of Na, K, and Ca in both flame atomic absorption spectrometry and flame emission spectroscopy, allowing for detection of multiple wavelengths on the ms-timescale using a single channel detector [17]. Gamez and co-workers used the DMMA as an encoding device for compressed sensing spectral imaging of an atmospheric pressure plasma jet, which allowed for the evaluation of plasma emission for diagnostic analysis [18]. Ray *et al*. have used the DMMA as a method of spatially modulating emission from an inductively coupled plasma as a means of detecting non-spectroscopic matrix effects (Ray, in preparation).

In this work, the DMMA is used for temporal gating and spatial filtering in the LIBS and LAMIS experiments for the first time. The efficacy and speed of optical gating using the DMMA is evaluated, with LIBS spectra collected at various delay times and using multiple samples to demonstrate improved S/B achieved when using the device. The optical design is developed to achieve spatial filtering of the laser plasma, and the utility of spatial filtering is demonstrated by examining the spatial distribution of atomic and molecular emission features. Finally, the use of the device to detect isotopic emission shifts in graphite and uranium-doped glass samples using the LAMIS experiment is reported, and prospects for potential future use of this system in field portable devices are examined.

2. EXPERIMENTAL

2.1 Digital Micromirror Array

The DMMA used here was a DLP® LightCrafter™ 4500 Evaluation Module (Texas Instruments, Dallas, TX) which uses a DLP-4500 DMMA device possessing 1,039,680 mirrors in a 912 × 1140 array. Each mirror is 7.6 μm × 7.6 μm, and oriented on a diamond pattern with respect to the horizontal laboratory frame of reference (see Figure 1A). Mirrors are coated with aluminum to ensure high reflectivity and hermetically sealed behind glass that is 98% transmissive for wavelengths above 400 nm. Each mirror can be programmed to move to one of three states which reference three different mirror angles measured from the surface perpendicular: +12° (referred to as the 'ON' position), -12°, or 0° 'parked' (both referred to as the 'OFF' position). The manufacturer specifications report that each individual mirror is able to move between states in 5 μs [19].

The DMMA module was modified to expose the mirror array and operated using the accompanying DLPC350PROM software (Texas Instruments, Dallas, TX) over a USB connection. The images projected were 912 × 1140 pixel, 24-bit images (composed of three 8-bit images). Images were designed using Image J (National Institutes of Health, Bethesda, MD) and loaded into on-board FIFO firmware. An external trigger timing pulse was used to trigger the DMMA display driver, causing one 8-bit image to be loaded from the on-chip firmware of the DMMA and displayed on the surface of the DMMA. The image had a typical exposure time of 500 μs and a period of 1,000 μs. Optical alignment and image resolution were measured using a 1951 USAF image target illuminated with a mercury line source (Heath Company, Benton Harbor, MI).

2.2 LIBS and LAMIS

To perform the LIBS and LAMIS experiments, a Nd:YAG laser (Continuum Electro-Optics, Inc. Minilite II, Santa Clara, CA) was operated at the fundamental wavelength (1064 nm) or frequency quadrupled (266 nm), as specified in the text. The laser was operated at 3 Hz, with average energy of 24.9 ± 0.2 mJ/pulse at 1064 nm and 4.3 ± 1 mJ/pulse at 266 nm. The laser beam was focused onto the sample surface, resulting in measured average ablation crater diameters of 170 ± 10 μm when the laser operated at 1064 nm and 150 ± 20 μm when the laser operated at 266 nm. Crater size was measured by microscope photography (EO Industrial Non-Illuminated Stereo Microscope, Edmund Optics, Barrington, NJ) and analyzed using Image J software (NIH). The laser energy was monitored using a laser power meter (Power and Energy Meter, Scientech). Laser irradiance were calculated to be 17.4 ± 0.1 GW/cm^2 and 6.0 ± 0.1 GW/cm^2 for measurements with the 1064 nm and 266 nm laser lines, respectively. Both the Q-switch and the flash-lamps were triggered by a digital delay generator (Quantum Composers Plus Model 9518 Pulse Generator, Bozeman, MT) in order to synchronize the laser pulse with the DMMA.

A basic diagram of the experiment is shown in Figure 1B and 1C. The incoming beam was reflected via laser mirror (M1) and focused to a spot using fused silica lens (L1) (f = 75 mm) to form a LIBS plasma. The LIBS plasma emission was collected through a second fused silica lens (L2) (f = 40 mm) positioned perpendicular to the incoming beam, which imaged the plasma plume onto the DMMA surface located 109 mm away with a magnification = 2.1. The plasma emission was then re-imaged with a fused silica lens (L3) (f = 75 mm) positioned approximately 270 mm from the DMMA to reform the plasma image at the entrance slit of the spectrometer (magnification = 0.3). The 0.3-m focal length spectrometer (SR-303i-B Spectrograph, Andor Technology) and L3 were angled 12° from the L2/DMMA beam path to allow for temporal

gating by triggering the DMMA to the 'ON' position. When a mirror(s) in the array was positioned in the +12° 'ON' position, that portion of the plume image was reflected 12° from perpendicular to be redirected toward the spectrograph and detected. When a mirror(s) in the array remained in the 'parked' state or was toggled into the -12° in the 'OFF' position, that portion of the plume image was not directed towards the spectrograph and was not detected. In this way, the DMMA acted as a programmable optical gate. The spectrometer was equipped with an electron-multiplying CCD (EMCCD) (Newton^{EM}, Andor Technology) that was operated as a traditional CCD. The EMCCD was comprised of a 1600 pixel × 200 pixel array of 16 μm × 16 μm pixels. The spectrograph slit was set to 20.0 μm unless otherwise stated. A grating with 600 lines/mm (blazed at 500 nm) was used for the following experiments unless otherwise stated. The CCD was read out using the Andor Solis Acquisition software (Andor^{TM} Technology) and images processed using Origin (OriginLab, Northampton, MA).

A digital pulse delay generator was used to synchronize the experiment by supplying a trigger pulse to the laser flash-lamp, the laser Q-switch, and the DMMA. Due to the internal delay time of the DMMA processing hardware, synchronization of events occurred as shown in the timing diagram included as Figure S-2 in the supplemental information. First, the DMMA image processor was triggered to load the image onto the mirror array. During the processing delay of the DMMA, the laser flash-lamp was fired, and subsequently the laser Q-switch activated to initiate lasing. By appropriate choice of delay time, the laser pulse could be synchronized with the DMMA mirror change or could be delayed as noted in the text. The DMMA trigger in, DMMA trigger output, flash-lamp trigger, and Q-switch trigger were all monitored using a digital oscilloscope (GDS-1074B, GWInstek). The trigger output from the DMMA and signal from laser-light reflected off the DMMA surface to a fast diode detector

(DET36A, Thorlabs, Newton, NJ) were monitored to determine the delay between trigger-in and mirror 'ON' along with mirror translation speed.

3. RESULTS AND DISCUSSION

3.1 Temporal gating for LIBS measurement

To assess the temporal-gating capabilities of the DMMA for LIBS experiments, a pure copper sample was analyzed and emission spectra collected as a function of varying delay times between the LIBS laser pulse and DMMA mirror activation. In Figure 2, the spectra are plotted as a function of laser-to-mirror delay time, which represents the time delay between the DMMA change to the 'ON' state with respect to the laser pulse. Thus, negative laser-to-mirror delay times indicate that the mirror was changed to the 'ON' state before the laser pulse occurred, while positive laser-to-mirror delay times indicate the DMMA was gated to the 'ON' state after the laser pulse occurred. It should be noted that the DMMA acts as a gated integrating detector. As a result, the signal is an accumulation of all emission that occurred after the mirrors have been turned to the 'ON' state, where they remain for the duration of the LIBS plasma and relaxation. The length of the 'ON' state was 500 μs and was determined by the pattern exposure time specified in the DMMA computer software. Each LIBS spectrum is an accumulation of 500 laser shots using the 1064 nm fundamental wavelength of the laser.

The spectra in Figure 2 show the practical benefit of gated detection for LIBS signal acquisition. At negative laser-to-mirror delay times, the familiar broadband spectral background is observed in the form of an elevated baseline along with broad emission features (e.g. N II 500.5 nm). The continuum emission arises from electron-ion recombination and bremsstrahlung radiation, inherent to the formation of the laser-induced plasma [1]. At the laser-to-mirror delay time of 0 μs, a drastic decrease in continuum spectral background is observed. Atomic emission

lines (Cu I lines at 510.6 nm, 515.3 nm, 521.8 nm, 529.3 nm, and 578.2 nm) are observed across all delay times until the atomic emission dissipates at a laser-to-mirror delay time of 14 μs. The persistence of atomic emission into the 10 s of microseconds is expected and has been noted in the literature elsewhere [6, 11]. Due to the fact that the DMMA is an integrating detection scheme, the Cu I emission lines are observed in all spectra, even those with negative laser-to-mirror delay times. Although the ability to control gate width may be desired to ensure that emission after a certain time-point is not collected, several literature reports have shown that the gate width may a minimal contribution on the LIBS spectrum [12, 20].

To better determine the temporal response of the DMMA gating system, the laser was operated at 266 nm and the presence of the residual second harmonic laser line at 532 nm and emission from a copper sample were monitored as a function of different laser-to-mirror delay times. The 532-nm residual is a convenient estimation of the incoming laser pulse duration (FWHM = 7 ± 1 ns) that falls within the Cu I emission window for this spectrograph (see supplemental Figure S-2). In Figure 3A, the DMMA temporal response is plotted between -1 μs and 0 μs in 100 ns increments for the second harmonic laser line at 532 nm and emission from copper sample at Cu I 521.8 nm and Cu I 510.6 nm. Each point in Figure 3A is the average of 5 LIBS measurements, where each measurement represents accumulation of 20 laser shots. The time required for the second harmonic laser line (532 nm) to decrease from 10 – 90% of its maximum emission value, or temporal gating response, was measured to be 160 ± 80 ns. The poor shot-to-shot reproducibility associated with the laser second harmonic is evident, but does not compromise measurement of the DMMA instrument temporal response.

Figure 3B is a plot of the S/B versus the laser-to-mirror delay time for the Cu I emission lines at 510.6 nm, 515.3 nm, and 521.8 nm from the pure copper sample collected using a laser

wavelength of 1064 nm. *The purpose of gating detection in LIBS experiments is to reduce the contribution of spectral background to the emission measurement, and thus the S/B is an appropriate indicator of the efficacy of the approach.* As expected for LIBS experiments, the S/B is poor at early delay times due to the dominating broadband spectral background. The S/B then rapidly increases to a maximum, where the optimum spectra could be acquired. The optimum laser-to-mirror delay time is at 1 μs, and once the maximum S/B is reached, it begins to decrease until it approaches 0 at a laser-to-mirror delay time of 5 μs.

The DMMA detector temporal gating response measured here is much more rapid than the manufacturers specification, which is a 5 μs transition between mirror states [21]. The rapid temporal gating response is a consequence of the optical path used in the experiment, which redirects light reflected from the DMMA into the slit of the spectrograph placed 27-cm distant (see Figure 1). Each DMMA mirror requires 5 μs to move 12-degrees between OFF and ON states, and thus the angular velocity of an individual mirror is very high (2.4×10^6 degrees/s). The image of the LIBS plasma moves across the slit at a linear velocity of 9.94×10^6 mm/sec and sweeps a linear distance of 1.59 mm across the slit of the spectrograph in 160 ns. This temporal gating response corresponds well with the anticipated LIBS plasma size and demonstrates the speed of the temporal gating response.

In Figure 4, spectra acquired at -1 μs laser-to-mirror delay are compared to those acquired when a laser-to-mirror delay of 160 ns was used. In Figure 4A, an emission spectrum of the Cu sample at a laser-to-mirror delay time of -1 μs is shown. It is clear that the atomic emission lines of neutral copper are present along with significant broadband spectral background. The spectral background in Figure 4B (160 ns delay) is significantly lower as compared to Figure 4A. The signal-to-background ratio (S/B) was determined by dividing the net

signal of the emission line by the average intensity of 6 points from the background at ± 0.5 nm from the assessed line. The S/B of the Cu I emission peak at 521.8 nm improves from 2.1 in Figure 4A to 44.4 in Figure 4B, an improvement of 22 times. Similarly, Figures 4C and 4D show the results of an identical experiment conducted using pure silver as the sample. Much like in Figure 4A and 4B, a dramatic decrease in background is observed when comparing spectra with laser-to-mirror delay times of -1 μs and 160 ns, including the dissipation of the broad peak at 500 nm from the N II spectral background, resulting in an improvement in S/B of 6-times for the Ag I emission line at 546.5 nm.

3.2 Spatial Filtering

Another benefit of using the DMMA for detector gating is the ability to spatially filter the laser induced plasma emission dynamically, and in an arbitrary pattern. In order to obtain 2-D spatial and spectroscopic resolution using a conventional CCD polychromator, the optical source image is typically translated across the polychromator entrance slit, and individual 1-D monochromatic images used to reconstruct the overall source image. By contrast, this DMMA approach places the source image on the surface of the DMMA device before spectral analysis, and thus any spatial region of interest can be isolated and then spectroscopically analyzed based on the composition of the mirror mask. In this way spatial and spectral information from various locations within the plasma, including off-axis locations, can be collected without moving the plasma or the polychromator. This capability is useful in LIBS and LAMIS experiments. It is known that emission from atoms, ions, and molecules is observed at different times and in different regions of the laser-induced plasma [6, 22-24]. In general, the intensity of atomic emission increases with distance from the sample surface, where it eventually reaches a maximum emission value (e.g., between 0.5 mm and 1.5 mm for a copper sample depending on

laser irradiance) and decreases at longer distance (e.g., starting from maximum emission to between 1.5 mm to 3.0 mm depending on laser irradiance) from the surface [4]. Further, it has been shown by Glaus *et al.* the formation of polyatomic molecules that are important for the LAMIS experiment occurs with greatest abundance off-axis (between 0.2 mm to 0.7 mm from the sample, in a nitrogen atmosphere) from the incoming laser beam [5]. Thus, spatial filtering and plume imaging is of interest in both the study of the laser-plasma characteristics and in obtaining optimum S/B for the emission of interest [4, 25].

Because the optical design images the LIBS plasma onto the surface of the DMMA device, spatial filtering can be accomplished by using a set of masks to select different regions of the LIBS plasma image to be transmitted light to the spectrograph (*c.f.* Figure S-3). Sequential filtering was performed both vertically and horizontally across the plasma. For vertical spatial filtering, a set of 10 masks of 114 × 912 pixels corresponding to a 1.23 mm height across the DMMA surface (11.08 mm^2 area) were programmed to turn 'ON' while the rest of the DMMA remained in the 'OFF' position. For horizontal spatial filtering, a set of 9 masks of 1140 × 76 pixels corresponding to a 0.82 mm width (13.13 mm^2 area) were used.

The vertical and horizontal spatial resolution were evaluated using a back-illuminated USAF-1951 target and a Hg line source. The vertical spatial resolution was estimated by using image masks filter height of 54 μm for each filter the group 0 element 6 horizontal lines (1.78-l/mm) of the USAF-1951 target with 5 pixel-high lines corresponding to a. In Figure 5A, lines 280.62-μm wide are sufficiently resolved with a contrast of 72 ± 4%. The horizontal resolution was estimated using the group 0 element 1 vertical lines (1-l/mm) of the USAF-1951 target with 6 pixel-wide lines corresponding to a filter width of 64.8 μm for each line. Figure 5B demonstrates that lines 500-μm wide are sufficiently imaged with a contrast of 90 ± 10%.

Although this suggests that horizontal spatial filtering of features down to 250-µm are achievable, there are limitations that arise with horizontal imaging. As shown in Figure 5B, formation of the image at the slit to the spectrometer results in poorer image transfer for image locations off the central axis of the slit, distorted the intensity of each line. Presumably, this might be rectified using a dedicated flat-field image: however, this simple image transfer was deemed sufficient for the purpose of this demonstration.

Results from spatial filtering the laser-induced plasma can be seen in Figure 6. A yttrium sample was used to assess the ability of the device for spatial filtering, as yttrium is known to show strong oxide molecular emission bands. Figure 6A represents the emission spectra resulting from horizontal spatial filtering. The spectra are normalized to the emission intensity of the Y I emission line at 567.5 nm. For ease of viewing and comparison, the ratio of emission from YO at bandhead at 613.3 nm to the emission of the Y I emission line at 567.5 nm are plotted as a function as the distance from the right edge of the DMMA surface and can be seen in Figure 6B. It is clear that, as expected, YO dominates emission spectra at the left and right edges of the laser-induced plasma. This is to be expected as this is where the atomic Y has the highest interaction with ambient oxygen. Additionally, we can see that the atomic emission dominates at the central regions of the laser-induced plasma. Again, this is to be expected as this is where the plasma temperatures are highest, and little interaction between ablated species and the ambient atmosphere occur. Similarly, Figure 6C demonstrates the vertical emission profile of the laser-induced plasma at t_D of both 160 ns and 6 µs. As expected, at t_D=160 ns, emission resulting from the YO bandhead is low until it increases at heights nearing the plasma edge. The locations highest above the sample surface show the greatest emission from YO which would correspond to the area with the most interaction with ambient environment. The spatial emission profile of Y

emission reveals the quick dissipation of the Y atomic and ionic emission and the persistence of the YO emission bands which are due to the formation of the YO species due to interactions with atmospheric gases, rather than YO being ablated from the surface of the Y sample [22-24, 26].

Figure 7 contains 2-dimensional spatial emission maps that were generated using 36 individual masks sampling regions of interest 152 pixels × 190 pixels, corresponding to an 'ON' width of 1.64 mm and an 'ON' height of 2.05 mm (3.37 mm^2 area), that were collected in a sequential manner that permits image reconstruction. In this way, multiple elemental and molecular emission features can be monitored at defined specific spatial locations, or multiple locations recorded in a series in order to reconstruct spatial emission information. Figure 7A and 7B represent the spatial maps of emission from Y I at 567.5 nm and the YO bandhead at 597.3 nm at t_D of 160 ns, respectively. It is clear that emission from Y I is more intense than that of YO. Additionally, the emission of Y I is centered on the image area and at the center of the LIBS plume, as compared to the emission from YO suggesting the formation of YO from interaction of Y with ambient oxygen. Figure 7C, shows Y I emission at a t_D of 10 μs and the expected dissipation of atomic emission at this longer delay time. In Figure 7D, however, the long-lived YO emission at a t_D of 10 μs is clearly evident and has almost equivalent intensity as Figure 7B. Another noticeable feature of these emission maps is the double-lobe structure to the sides of the main LIBS plasma that can be seen in all of the images in Figure 7. This structure can be attributed to the splitting of the plume due to the formation of a vortex during collapse of the laser-induced plasma [6, 22].

3.3 LAMIS

The use of diatomic molecular emission for isotopic analysis (i.e., LAMIS) is particularly advantageous because the isotopic shift in diatomic molecular band is magnified and can be

several orders of magnitude larger than that in atomic emission lines [2, 27] [27, 28]. As such, with LAMIS, optical isotopic analysis under atmospheric pressure for many elements is feasible. To demonstrate the efficacy of the DMMA as a temporal gating device for LAMIS experiments, UO and C_2 molecular bands were individually measured. For UO, a uranium glass sample was analyzed. Uranium glass typically contains anywhere from 0.1% to 2% uranium by weight with the natural isotopic distribution of ^{238}U (99.27%), ^{235}U (0.72%), and ^{234}U (0.01%). The spectra shown in Figure 8 were acquired with the laser operated at 266 nm, optimized for analysis of the glass [29]. At early t_D, an intense, broad peak resulting from the overlap of multiple uranium-based emission features is observed, with U II 593.2 nm, U I 593.4 nm, and UO 593.6 nm emission unresolved at the modest resolution of this spectrograph. Emission from phosphorus ions present in the glass at P II 602.4 nm, P II 603.4 nm, and P II 604.3 nm also rapidly dissipates (from 160 ns to 2 μs). At these early delay times, atomic, ionic and molecular emission features from uranium are convoluted, and thus the UO emission peak cannot be well characterized. As delay time increases, however, emission from ionic and atomic lines dissipates leaving only UO at a delay time of 8 μs. Molecular emission from UO was detected at all t_D in this sample since it is present in the glass and is persistent due also to the formation of UO resulting from interaction of uranium ions with atmospheric oxygen. The inability to distinguish between uranium isotopes is a result of the modest resolution of our spectrometer, but has been successfully reported elsewhere [27]. Recently, Chan and coworkers have also reported a computational approach that may permit use of partially-resolved spectroscopic data in assigning isotopic composition[28].

The C_2 Swan band emission from graphite with natural isotopic abundance and ^{13}C-enriched graphite were also acquired to demonstrate the isotopic shift in LAMIS spectra.

Figure 9 shows emission spectra from LAMIS analysis of graphite pellets where each spectrum represents a single laser shot and at a delay time of 4 μs. The isotopic shift between the molecular emission bands is clearly evident. The $^{12}C_2$ emission bandheads can be seen at 473.7 nm, 471.5 nm, and 469.7 nm corresponding to the C_2 (1,0), C_2 (2,1), and C_2 (3,2) transitions, respectively. The isotopic shift is clearly evident based on the corresponding bands can be seen for $^{13}C_2$ emission at 475.2 nm, 473.0 nm, and 471.2 nm, respectively [30]. Rotational fine structure within individual vibronic modes of the C_2 emission cannot be resolved with the modest resolution of our spectrometer, however, the shift in band head location is clear [2].

4. CONCLUSIONS

The current work demonstrates the ability of a DMMA to temporally gate emission spectra for LIBS and LAMIS experiments. Atomic emission, molecular emission, and continuum background from the LIBS plasma were detected with a temporal response as short as 160 ns. LIBS spectra showed a signal-to-background ratio (S/B) improvement of up to 22 times when DMMA-gated detection was employed. The ability of the DMMA device to spatially filter emission from the LIBS/LAMIS plasma was also demonstrated. Detectability of specific emission features of interest was improved based on observation delay time and location, with atomic emission features optimized at central locations within the plasma and at short delay times as compared to molecular emission features which were found at the edges of the LIBS plasma and to occur at longer delay times. The ability to incorporate the DMMA into LAMIS experiments was also demonstrated. Isotopic emission shift in the Swan band emission due to $^{12}C_2$ and $^{13}C_2$ was observed and optimized for detection using this DMMA approach. The emission band resulting from UO from a uranium glass matrix was also detected in anticipation

of isotopic analysis in future studies. The reported results presented here hold promise that such a device might be included in handheld devices in future.

Acknowledgements

This paper is included within an issue dedicated to Dr. Rick Russo, honoring his significant contributions to atomic spectroscopy research. The authors would like to acknowledge their debt to Dr. Russo for many insightful comments and suggestions over a period of many years, for his collegial and upstanding nature, and for providing an example of excellence throughout his career as a research leader. This research was supported by The State University of New York at Buffalo and by the US Department of Energy, Office of Defense Nuclear Nonproliferation Research and Development, under contract number DE-AC02-05CH11231 at the Lawrence Berkeley National Laboratory (LBNL).

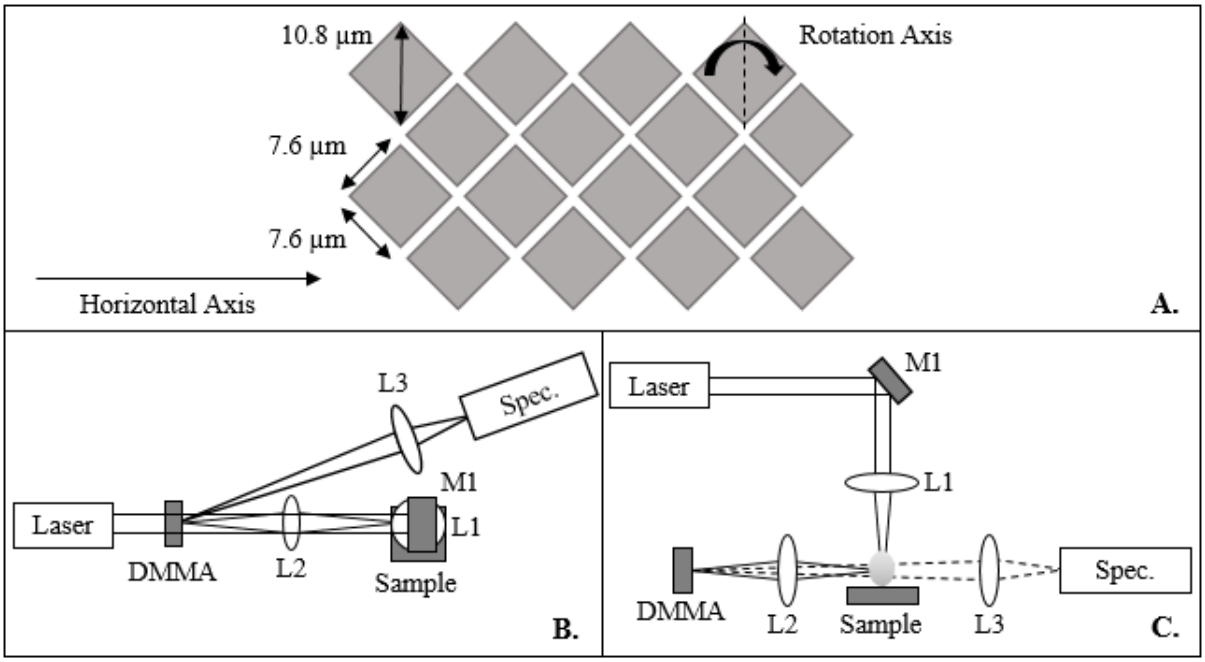

Figure 1. **A.** Diagram of micromirror array layout. Grey diamonds represent individual micromirrors. **B.** Top-down view of the experimental setup. L3 and the spectrograph are offset 12° from the emission beam path from the plasma to the DMMA to facilitate temporal gating using the DMMA. **C.** Side-on view of the experimental setup. (Figures not drawn to scale for ease of viewing.

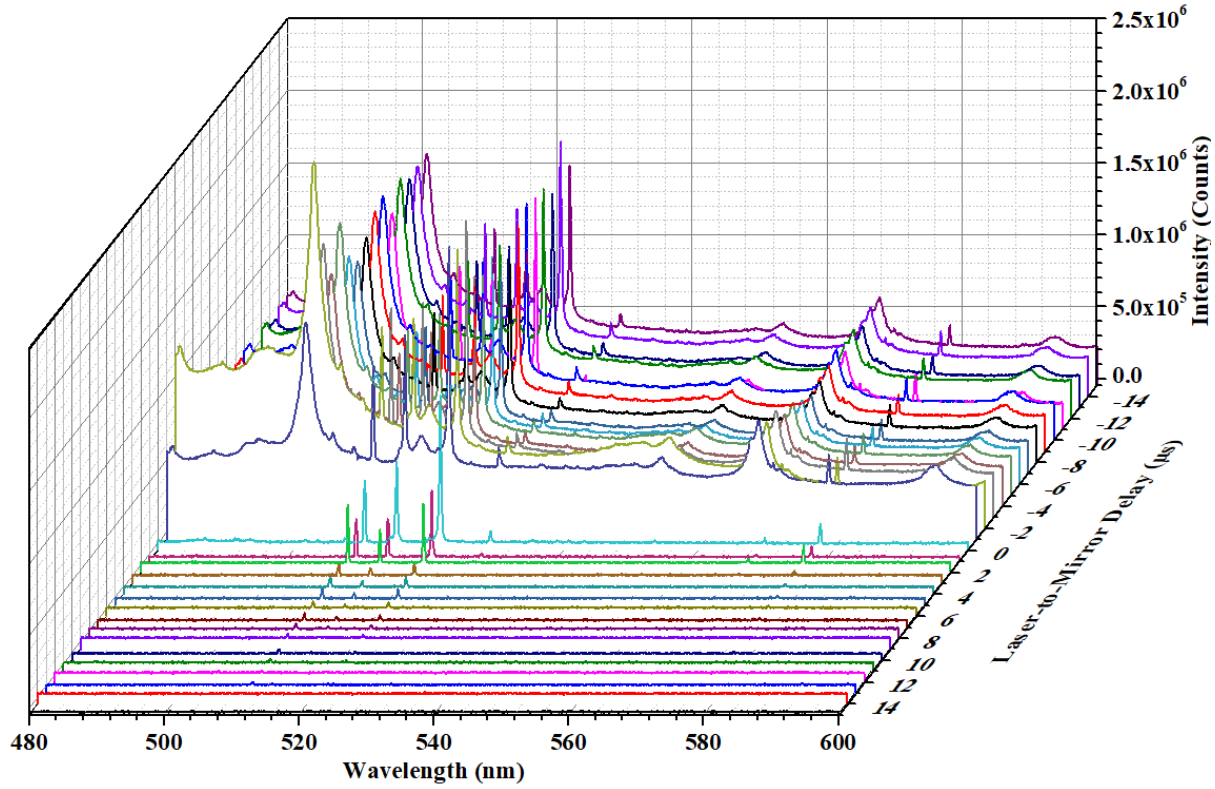

Figure 2. DMMA-gated LIBS spectra of a pure copper sample in 1 μs increments. Each spectrum is a result of 500 laser shots accumulated. All emission lines result from atomic emission of Cu.

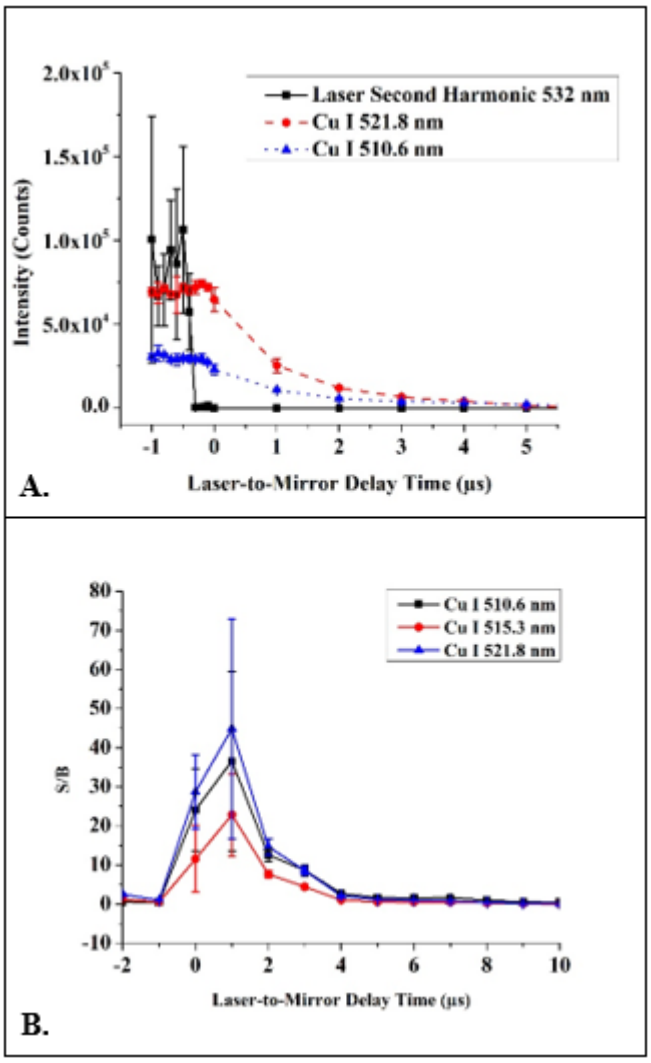

Figure 3. A. Plot of line intensity versus t_D. The intensity of the laser second harmonic is plotted along with copper atomic emission lines at 510.6 nm and 521.8 nm to demonstrate the difference in persistence of these two lines. Error bars represent the standard deviation resulting from 5 measurements. **B.** Plot of S/B versus the laser-to-mirror delay time for Cu I emission at 510.6 nm, 515.3 nm, and 521.8 nm. Error bars represent the standard deviation of 3 replicate measurements. The background is taken as the average of 3 points on either side of the emission peak that do not contain any additional spectral features.

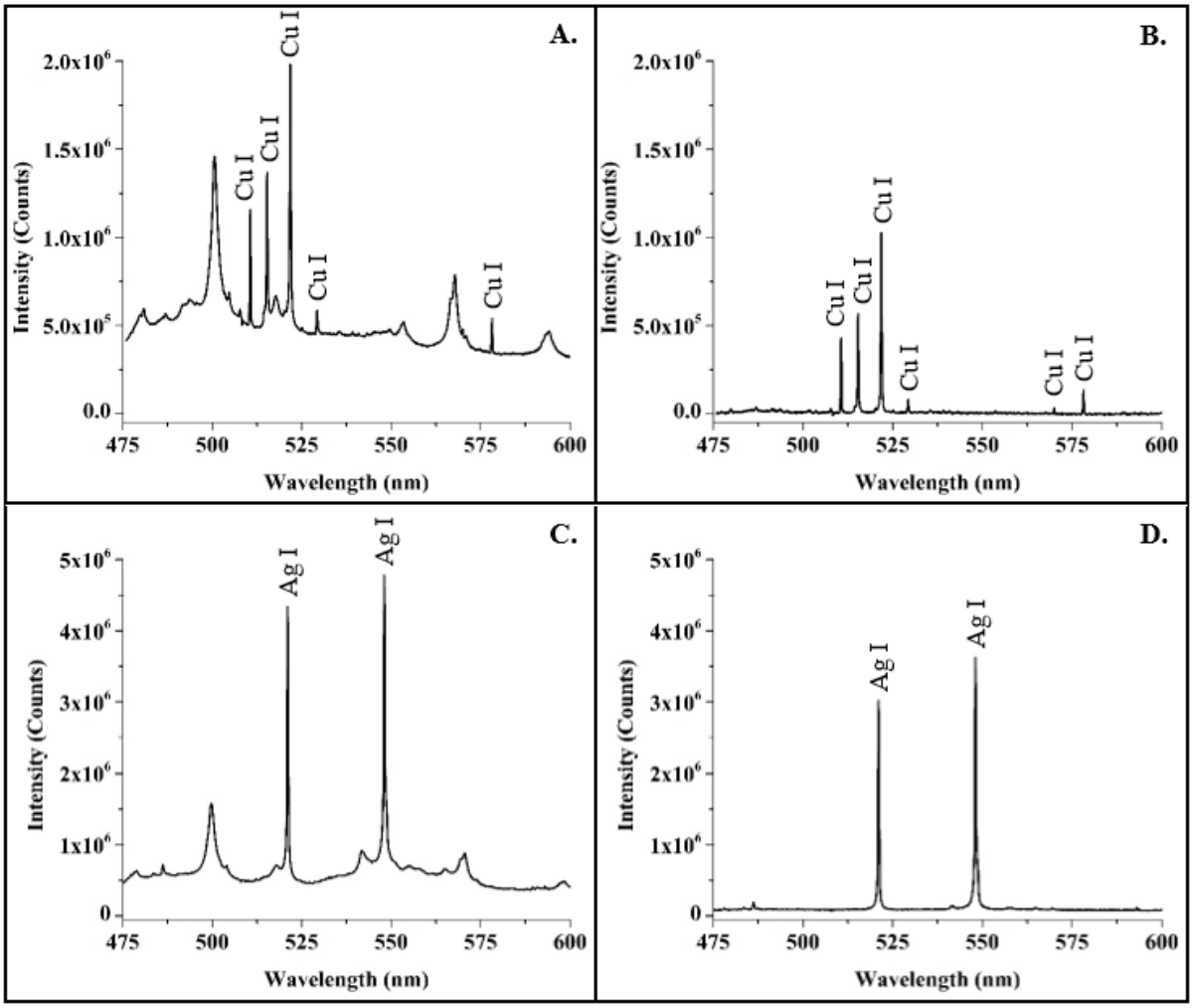

Figure 4. Time-resolved LIBS spectra of **A.** copper at laser-to-mirror delay time of -1 µs, **B.** copper at laser-to-mirror delay time of 160 ns, **C.** silver at laser-to-mirror delay time of -1 µs, and **D.** silver at laser-to-mirror delay time of 160 ns.

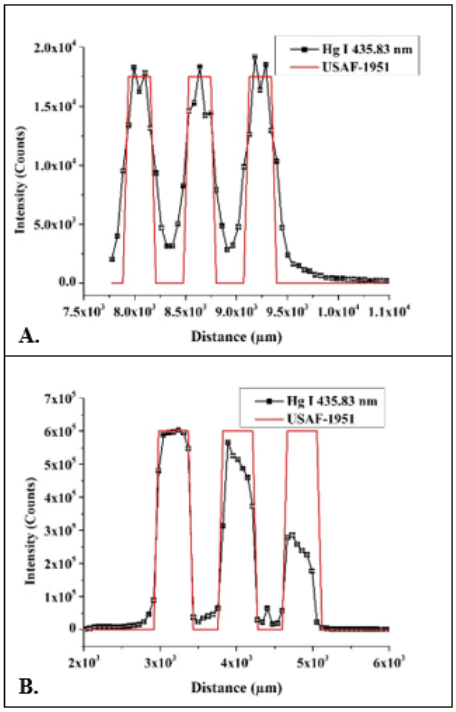

Figure 5. Recreation of USAF-1951 target **A.** group 0 element 6 horizontal line image using 54.0 μm vertical filters and **B.** group 0 element 1 vertical line image using 64.8 μm horizontal filters. Each point is an average of 3 spectra.

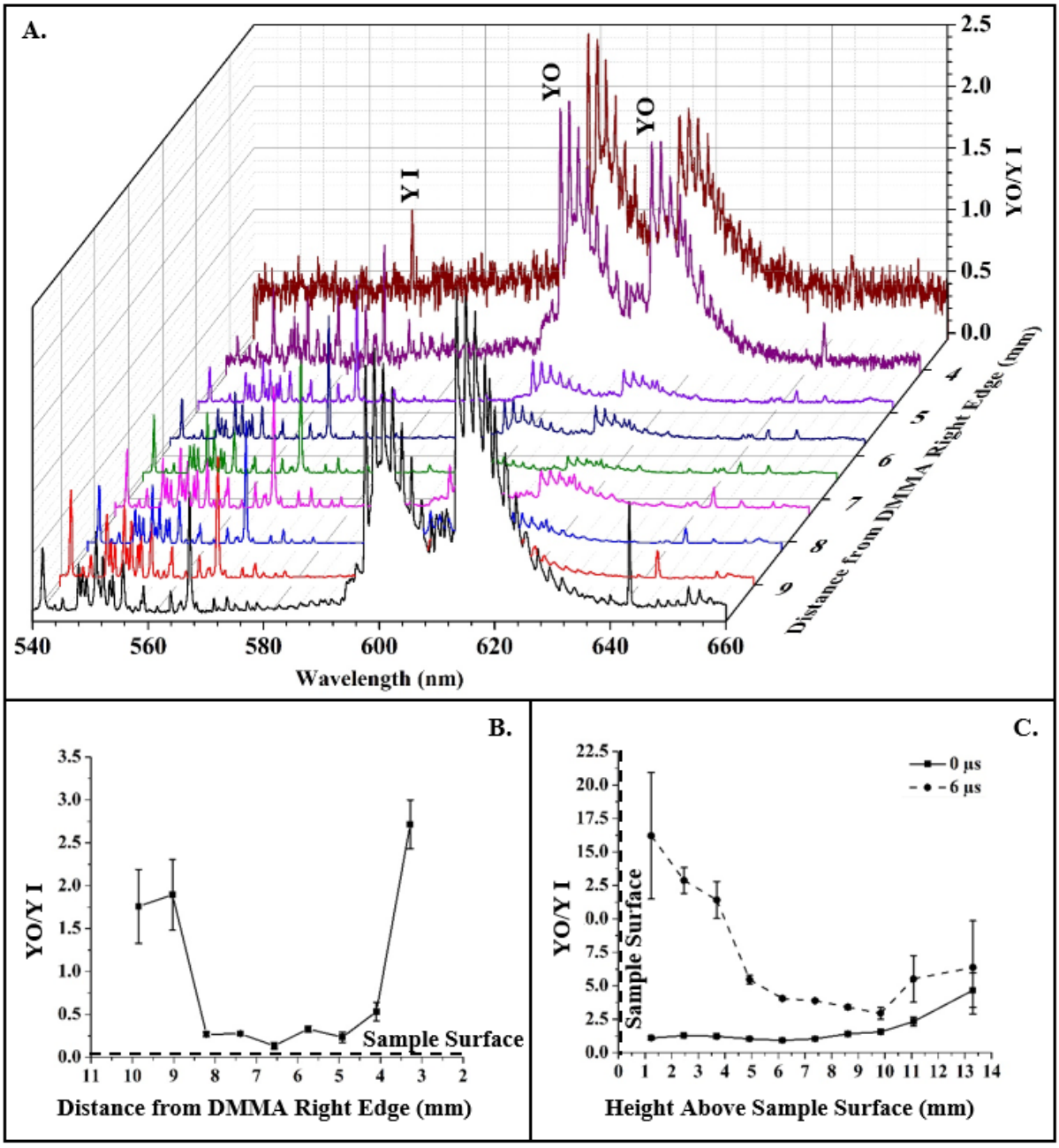

Figure 6. Result of spatially filtering laser-induced plasma emission from a yttrium sample. The ratio of the emission from the YO emission bandhead at 613.3 nm and the Y I emission line at 567.5 nm for the **A.** horizontal spatially filtered emission with t_D of 0 µs and **B.** vertically filtered emission at t_D of 0 µs and 6 µs. Error bars represent the standard deviation of 3 replicate measurements. **C.** horizontal spatially filtered emission spectra with t_D of 160 ns. All emission is normalized to the emission from Y I at 567.5 nm.

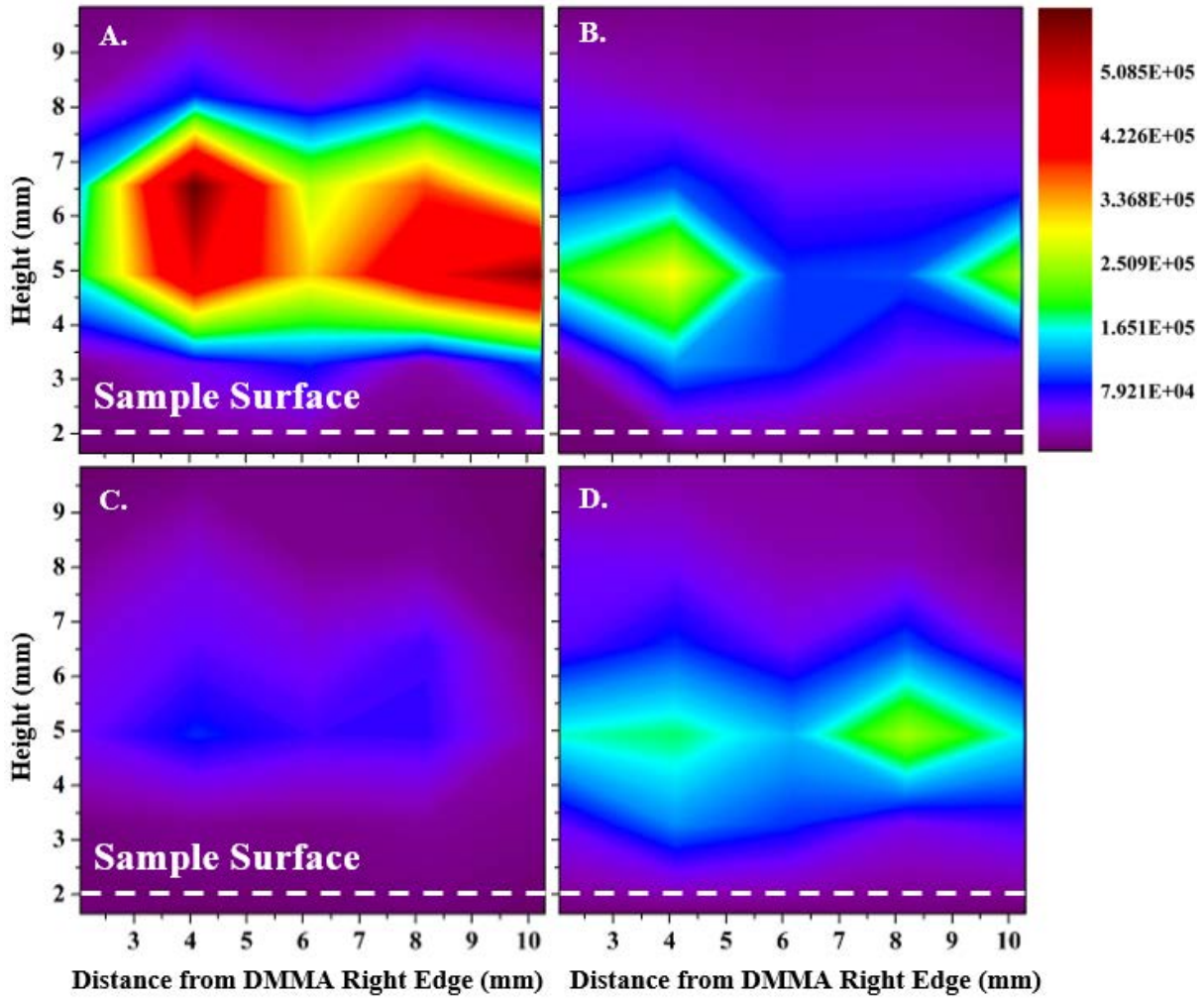

Figure 7. Map of emission from **A.** Y I at 567.5 nm and **B.** the YO bandhead at 597.3 nm at t_D 160 ns as well as emission from **C.** Y I and **D.** the YO bandhead at t_D 10 µs.

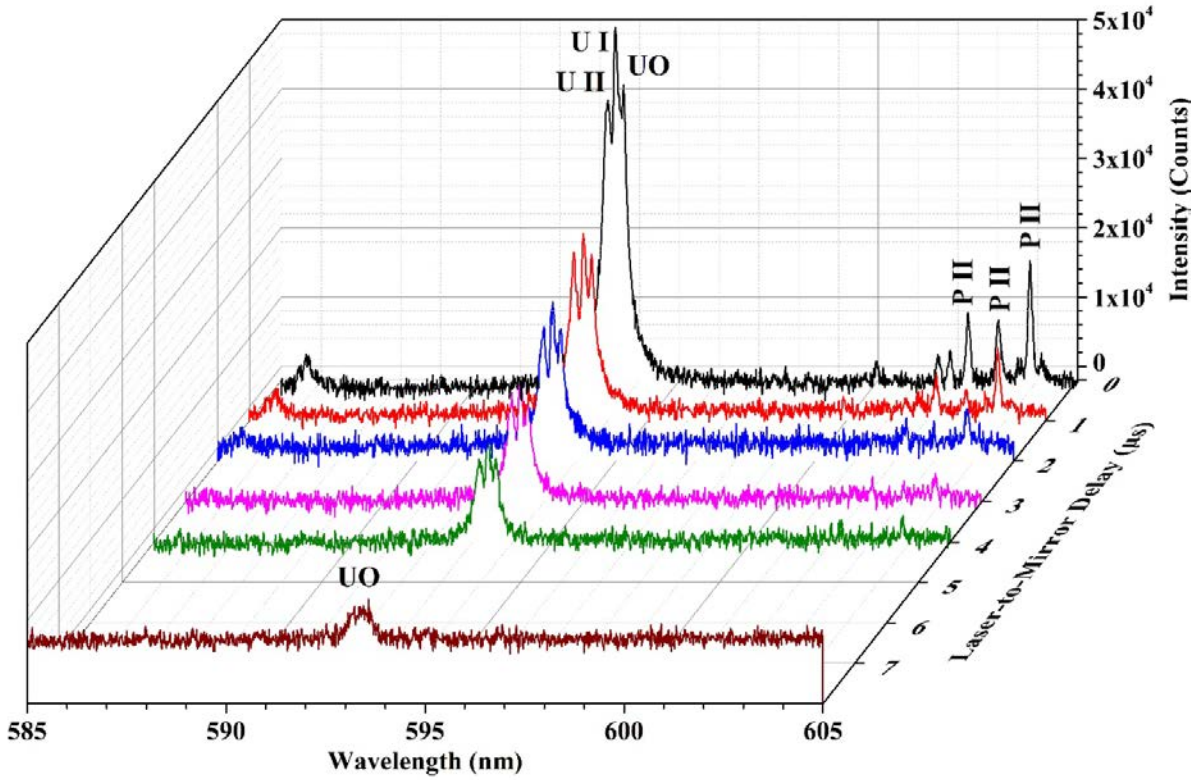

Figure 8. Emission spectra resulting from analysis of a fragment of a uranium glass plate. Each spectrum is an average of 3 spectra composed of 100 laser shots.

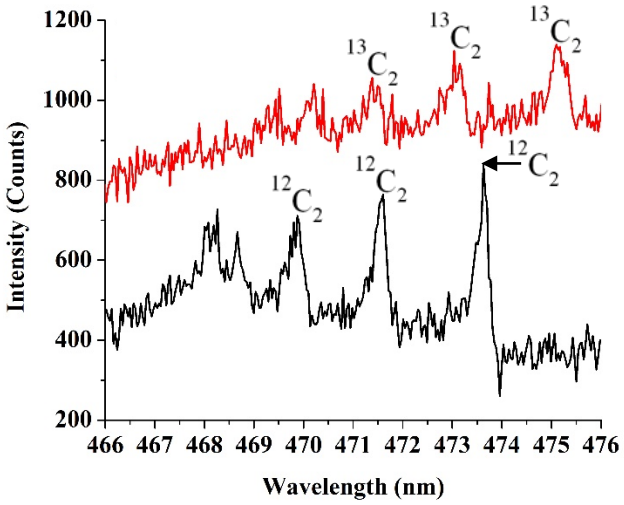

Figure 9. $^{12}C_2$ and $^{13}C_2$ spectra from analysis of graphite pellets. Emission spectra result from a single shot measurement. The $^{13}C_2$ spectrum is offset 400 counts for ease of viewing.

REFERENCES

[1] D.W. Hahn, N. Omenetto, Laser-Induced Breakdown Spectroscopy (LIBS), Part I: Review of Basic Diagnostics and Plasma-Particle Interactions: Still-Challenging Issues Within the Analytical Plasma Community, Applied Spectroscopy, 64 (2010) 335A - 366A.

[2] R.E. Russo, A.A. Bol'shakov, X. Mao, C.P. McKay, D.L. Perry, O. Sorkhabi, Laser Ablation Molecular Isotopic Spectrometry, Spectrochimica Acta Part B, 66 (2011) 99-104.

[3] X. Mao, A.A. Bol'shakov, D.L. Perry, O. Sorkhabi, R.E. Russo, Laser Ablation Molecular Isotopic Spectrometry: Parameter Infulence on Boron Isotope Measurments, Spectrochimica Acta Part B, 66 (2011) 604 - 609.

[4] X.L. Mao, M.A. Shannon, A.J. Fernandez, R.E. Russo, Temperature and Emission Spatial Profiles of Laser-Induced Plasmas During Ablation Using Time-Integrated Emission Spectroscopy, Applied Spectroscopy, 49 (1995) 1054 - 1062.

[5] R. Glaus, J. Riedel, I. Gornushkin, Insight into the Formation of Molecular Species in Laser-Induced Plasma of Isotopically Labeled Organic Samples, Analytical Chemistry, 87 (2015) 10131 - 10137.

[6] S.S. Harilal, B.E. Brumfield, B.D. Cannon, M.C. Phillips, Shock Wave Mediated Plume Chemistry for Molecular Fomration in Laser Ablation Plasmas, Analytical Chemistry, 88 (2016) 2296 - 2302.

[7] M.S. Rabasovic, B.P. Marikovic, D. Sevic, Time-Resolved Optical Spectra of the Laser-Induced Indium Plasma Detected Using a Streak Camera, IEEE Transactions on Plasma Science, 42 (2014) 2588 - 2589.

[8] R.E. Neuhauser, B. Ferstl, C. Haisch, U. Panne, R. Niessner, Design of a Low-Cost Detection System for Laser-Induced Plasma Spectroscopy, Review of Scientific Instruments, 70 (1999) 3519 - 3522.

[9] T. Sakka, K. Irie, K. Fukami, Y.H. Ogata, Emission Spectroscopy of Laser Ablation Plasma with Time Gating by Acousto-Optic Modulator, Review of Scientific Instruments, 82 (2011) 023112-023111 - 023112-023117.

[10] J.E. Carranza, E. Gibb, B.W. Smith, D.W. Hahn, J.D. Wineforder, Comparison of Nonintensified and Intensified CCD Detectors for Laser-Induced Breakdown Spectroscopy, Applied Optics, 42 (2003) 6016 - 6021.

[11] M. Mueller, I.B. Gornushkin, S. Florek, D. Mory, U. Panne, Approach to Detection in Laser-Induced Breakdown Spectroscopy, Analytical Chemistry, 79 (2007) 4419 - 4426.

[12] M.T. Taschuk, Y. Godwal, Y.Y. Tsui, R. Fedosejevs, M. Tripathi, B. Kearton, Absolute Characterization of Laser-Induced Breakdown Spectroscopy Detection Systems, Spectrochimica Acta Part B, 63 (2008) 525 - 535.

[13] P. Pořízka, B. Klessen, J. Kaiser, I. Gornushkin, U. Panne, J. Riedel, High Repetition Rate Laser-Induced Breakdown SpectroscopyUisng Acousto-Optically Gated Detection, Review of Scientific Instruments, 85 (2014) 073104-073101 - 073104-073108.

[14] L. Streeter, G.R. Burling-Claridge, M.J. Cree, R. Künnemeyer, Visible/Near Infrard Hyperspectral Imaging Via Apatial Illumination Source Modulation, Journal of Near Infrared Spectroscopy, 15 (2007) 395 - 399.

[15] S. Singh-Gasson, R.D. Green, Y. Yue, C. Nelson, F. Blattner, M.R. Sussman, F. Cerrina, Maskless Fabrication of Light-Directed Oligonucleotied Microarrays Using a Digital Micromirror Array, Nature Biotechnology, 17 (1999) 974 - 978.

[16] T.M. Spudich, C.K. Utz, J.M. Kuntz, R.A. DeVerse, R.M. Hammaker, D.L. McCurdy, Potential for Using a Digital Micromirror Device as a Signal Multiplexer in Visible Spectroscopy, Applied Spectroscopy, 57 (2003) 733 - 736.

[17] J.D. Batchelor, B.T. Jones, Development of a Digital Micromirror Spectrometer for Analytical Atomic Spectroscopy, Analytical Chemistry, 70 (1998) 4907 - 4914.

[18] J.D. Usala, A. Maag, T. Nelis, G. Gamez, Compressed Sensing Spectral Imaging for Plasma Optical Emission Spectroscopy, Journal of Analytical Atomic Spectrometry, 31 (2016) 2198 - 2206.

[19] DLP4500 (0.45 WXGA DMD), in, Texas Instruments, Dallas, TX, 2018.

[20] J.-B. Sirven, P. Mauchien, B. Sallé, Analytical Optimization of Some Parameters of a Laser-Induced Breakdown Spectroscopy Experiment, Spectrochimica Acta Part B, 63 (2008) 1077 - 1084.

[21] DLP4500 .45 WXGA DMD Datasheet, in, Texas Instruments, 2019.

[22] P. Ran, H. Hou, S.-N. Luo, Molecule Formation Induced by Non-uniform Plume-air Interactions in Laser Induced Plasma, Journal of Analytical Atomic Spectrometry, 32 (2017) 2254 - 2262.

[23] A. Matsumoto, H. Ohba, M. Toshimitsu, K. Ankaoka, A. Ruas, I. Wakaida, T. Sakka, S. Yae, Enhancement of Molecular Formation in Fiber-optic Laser Ablation with a Long Nanosecond Pulsed Laser, Spectrochimica Acta Part B, 155 (2019) 56 - 60.

[24] David G. Weisz, J.C. Crowhurst, M.S. Finko, T.P. Rose, B. Koroglu, R. Trappitsch, H.B. Radousky, W.J. Siekhaus, M.R. Armstrong, B.H. Isselhardt, M. Azer, D. Curreli, Effects of Plume Hydrodynamics and Oxidation on the Composition of a Condensing Laser-Induced Plasma The Journal of Physical Chemistry A, 122 (2018) 1584 - 1591.

[25] A. De Giacomo, Experimental Characterization of Metallic Titanium-Laser Induced Plasma by Time and Space Resolved Optical Emission Spectroscopy, Spectrochimica Acta Part B, 58 (2003) 71 - 83.

[26] S.S. Harilal, R.C. Issac, C.V. Bindhu, V.P.N. Nampoori, C.P.G. Vallabhan, Temporal and Spatial Evolution of C_2 in Laser Induced Plasma from Graphite Target, Journal of Applied Physics 80 (1996) 3561 - 3565.

[27] X. Mao, G.C.-Y. Chan, I. Choi, V. Zorba, R.E. Russo, Combination of Atomic Lines and Molecular Bands for Uranium Optical Isotopic Analysis in Laser Induced Plasma Spectrometry, Journal of Radioanalytical Nuclear Chemistry, 312 (2017) 121 - 131.

[28] G.C.-Y. Chan, X. Mao, I. Choi, A. Sarkar, O.P. Lam, D.K. Shuh, R.E. Russo, Multiple Emission Line Analysis for Improved Isotopic Determination of Uranium - A Computer Simulation Study Spectrochimica Acta Part B, 89 (2013) 40 - 49.

[29] D.W. Hahn, N. Omenetto, Laser-Induced Breakdown Spectroscopy (LIBS), Part II: Review of Instrumental and Methodological Approaches to Material Analysis and Applications to Different Fields, Applied Spectroscopy, 66 (2012) 347 - 419.

[30] M. Dong, G.C.-Y. Chan, X. Mao, J.J. Gonzalez, J. Lu, R.E. Russo, Elucidation of C_2 and CN Formation Mechanisms in Laser-Induced Plasmas Through Correlation Analysis of Carbon Isotopic Ratio, Spectrochimica Acta Part B, 100 (2014) 62 - 69.

SUPPLEMENTAL INFORMATION:

"The Use of a Digital Micromirror Array as a Temporal Gate and Spatial-Filtering Device for Laser-Induced Breakdown Spectroscopy and Laser Ablation Molecular Isotopic Spectrometry"

Kelsey L. Williams[1], George C.-Y. Chan[2], and Steven J. Ray[1*]

[1]The State University of New York at Buffalo, Buffalo, New York 14260, United States

[2]Lawrence Berkeley National Laboratory, Berkeley, California 94720, United States

* Author to whom correspondence should be addressed: sjray2@buffalo.edu

SUPPLEMENTAL INFORMATION

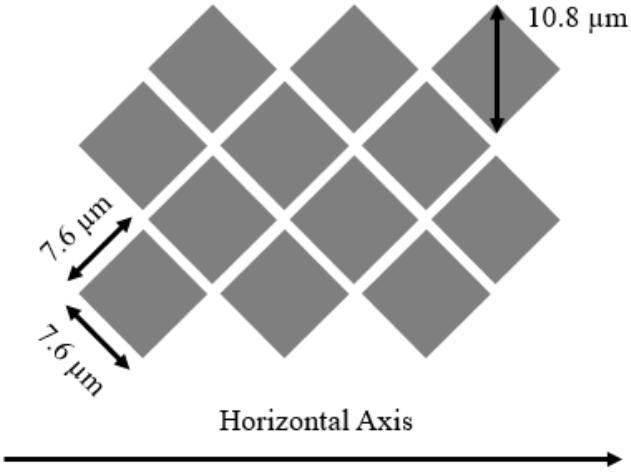

Figure S-1. Diagram of micromirror array layout. Grey diamonds represent individual micromirrors.

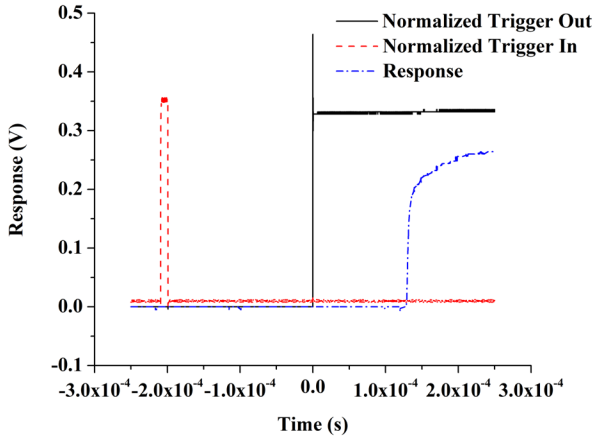

Figure S-2. Plot of the DMMA response to an external trigger. The Trigger In and Trigger Out are normalized with respect to the DMMA response. The Trigger In period was 1 s, with an 'ON/OFF' pattern period and exposure time of 10 ms.

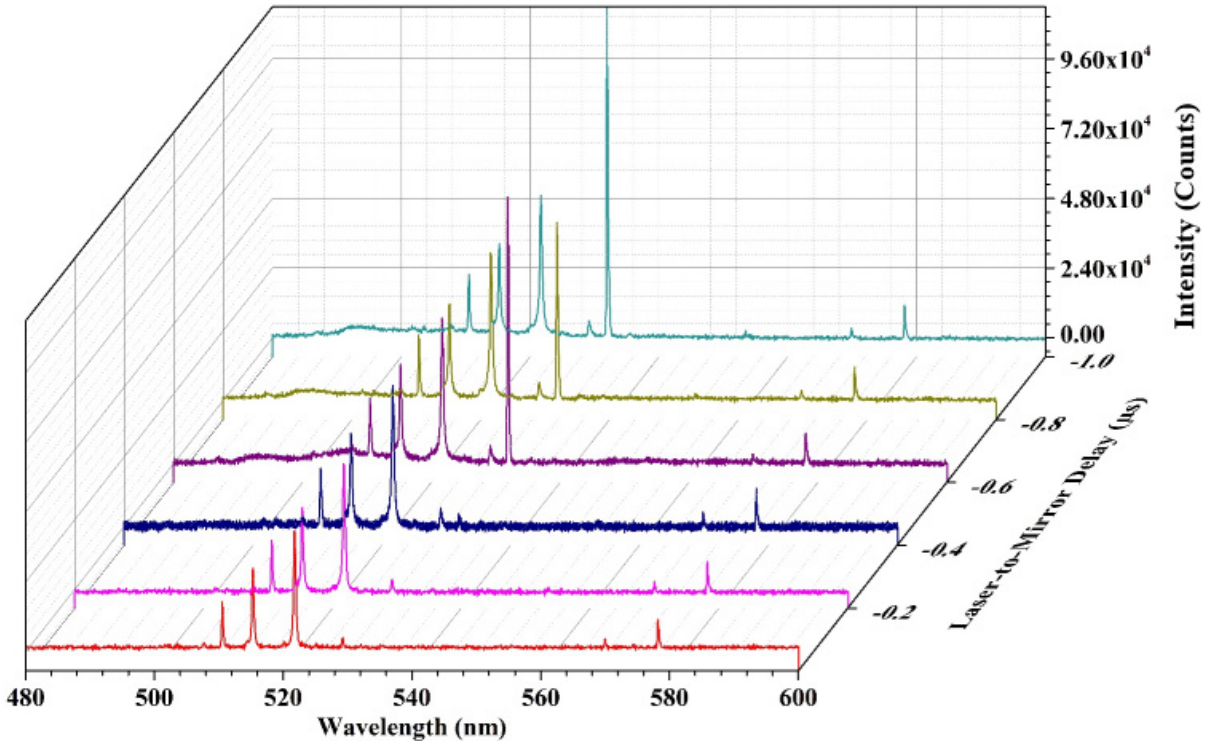

Figure S-3. 3-D plot of LIBS spectra of pure copper at various t_D with the laser operated at 266 nm. All lines result from Cu(I) emission, except the rapidly dissipating line at 532 nm, which is a result of the laser second harmonic.

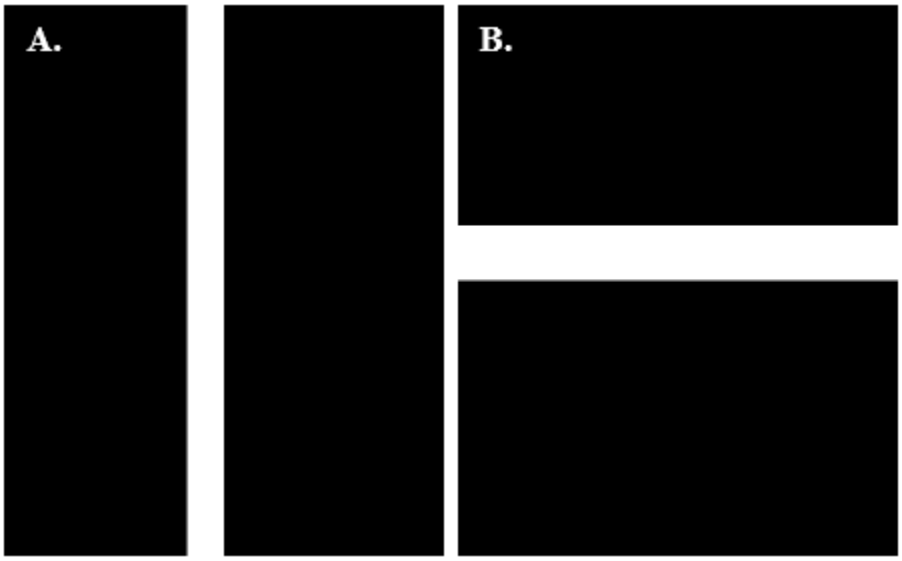

Figure S-4. Examples of masks for **A.** horizontal and **B.** vertical spatial filtering. These images were loaded to the surface of the DMMA. The white portion of the image is the area of the 'ON' mirrors where the black portions are the 'OFF' areas.